A Particle Filtering-Based Magnetic Field Map Generation Method Using Smartphones

Shiyi Chen^{1,2}, Tingwei Wang¹, Jian Kuang^{1,†}, Xiaoji Niu^{1,3}

the GNSS Research Center, Wuhan University, Wuhan 430079, China
 the School of Geodesy and Geomatics, Wuhan University, Wuhan 430079, China
 the Hubei Luojia Laboratory, Wuhan, Hubei 430079, China

Keywords: Indoor Positioning, Magnetic Field Matching, Magnetic Field Map Generation, Particle Filtering.

Abstract

Magnetic field matching has emerged as one of the mainstream indoor positioning methods due to its independence from base stations and its resilience to interference. A critical factor influencing magnetic field matching is the magnetic field map, and the challenge lies in generating a high-precision magnetic field map efficiently and cost-effectively. This paper proposes a method for magnetic field map generation based on particle filtering. This approach requires data collectors to traverse the same route repeatedly, using Pedestrian Dead Reckoning (PDR) to estimate trajectories and employing the horizontal and vertical components of the magnetic field to detect when users return to historical positions, thereby controlling position error accumulation. Furthermore, by leveraging the post-processing characteristics of the magnetic field map, all particles are retrospectively analyzed, significantly enhancing the accuracy of trajectory estimation. Subsequently, four non-colinear control points are used to calibrate the relative trajectories, and bilinear interpolation is employed to generate a grid magnetic field map. Experimental results demonstrate that the proposed method achieves a root mean square (RMS) positioning error of less than 1.3 m, meeting the requirements for meter-level magnetic field matching positioning. The generated magnetic field map exhibits errors of 30-40 mGauss in the northward, eastward, and vertical directions.

1. Introduction

With the proliferation of the Internet of Things (IoT) and smartphones, location-based service (LBS) is playing an increasingly crucial role in people's everyday activities, including indoor security, targeted advertising, and indoor navigation. For LBS, acquiring precise location information is essential. In outdoor environments, Global Navigation Satellite System (GNSS) can provide precise positioning service. However, GNSS is ineffective indoors due to signal obstructions, presenting a significant challenge in achieving accurate and reliable location estimation

In recent years, various indoor positioning solutions have been developed, categorized into relative and absolute positioning methodologies. Relative positioning systems primarily include Simultaneous Localization and Mapping (SLAM) techniques and dead reckoning (Guo et al., 2020). SLAM approaches, such as visual SLAM (Campos et al., 2021) and LiDAR SLAM (Huang, 2021), demonstrate high precision in feature-abundant environments. However, visual SLAM necessitates optimal lighting conditions and distinct visual features, while LiDAR SLAM requires expensive hardware and substantial computational resources. Moreover, both methods exhibit limitations in dynamic environments and lack global localization capabilities. Similarly, dead reckoning systems suffer from cumulative errors, primarily serving as supplementary positioning aids. Absolute positioning primarily relies on wireless and environmental signal fingerprinting, encompassing various technologies such as cellular networks, WiFi (Tinh and Hoang, 2022), Bluetooth Low Energy (BLE) (Jianyong et al., 2014), and magnetic field strength (Kuang et al., 2023). Among these, 3G and 4G positioning accuracy

is relatively low, whereas 5G positioning offers enhanced accuracy through time difference of arrival (TDOA) analysis, its limited coverage restricts widespread application. WiFi-based positioning leverages existing infrastructure but faces accuracy challenges from environmental interference. BLE systems require extensive beacon deployment and are similarly affected by indoor obstacles. In contrast, magnetic field matching positioning utilizes stable indoor magnetic field signatures created by ferromagnetic material interactions with geomagnetic fields (Kuang et al., 2018). This approach requires no additional infrastructure and maintains long-term stability, making it currently the most cost-effective and practical indoor positioning solution.

The magnetic field map is fundamental in the magnetic field matching, and its accuracy directly determines the precision of magnetic field matching. Therefore, the generation of the magnetic field map is crucial. Currently, manual collection is the most prevalent method for collecting magnetic field maps. The approach involves using specific surveying techniques to obtain high-precision position coordinates, which is then associated with collected magnetic field information to form a "magnetic field-position" correspondence (Kuang et al., 2021). The accuracy of this approach mainly depends on the precision of position coordinate measurements. Current magnetic field map generation methods may require deploying numerous control points, and as the area and complexity of the scene increase, traditional manual collection methods become inconvenient and labour-intensive in many scenarios.

In response, we address the challenges of manual magnetic field map collection by designing a particle filtering-based magnetic field map generation method us-

ing smartphones in this paper. This method employs a particle filtering framework, leveraging position estimates from PDR as prior information. It implements closed-loop detection based on magnetic field fingerprint features to effectively suppress PDR position drift. Finally, it utilizes particle backtracking to eliminate invalid particles, achieving a more accurate trajectory. On this basis, the integration of a small number of control points and bilinear interpolation enables the generation of the magnetic field map.

The remainder of this paper is structured as follows: Section 2 reviews the relevant previous works. Section 3 provides an overview of the proposed methods. Section 4 detail magnetic field map generation method based on particle filtering. Section 5 discusses the experiments and results. Finally, the conclusion and future work are presented in Section 6.

2. Relate work

The presence of reinforced concrete in building materials causes distortions in the geomagnetic field within indoor environments, resulting in the emergence of a distinctive environmental magnetic field. Additionally, given that the structural composition of reinforced concrete within buildings remains unchanged over prolonged periods, the characteristics of the environmental magnetic field remain stable over time (Ashraf et al., 2020). The precision of the magnetic field map significantly influences the precision of the magnetic field matching. The objective of constructing a magnetic field map is to establish the correspondence between location and the three-dimensional vectors of the magnetic field within an area. Typically, the consumer-grade magnetometers embedded in smartphones are sufficient in terms of accuracy and sampling rate to meet the requirements for magnetic field map generation.

Presently, the methods for collecting magnetic field maps are predominantly manual, including point collection (Galván-Tejada et al., 2014) (Liu et al., 2021), line collection (Ouyang and Abed-Meraim, 2022), crowdsourcing, and simultaneous localization and mapping (SLAM). In point collection, indoor areas are segmented into several smaller regions where data collection is performed. This method incurs high costs, and the difficulty of collection escalates with the expansion of the collection area, making it suitable only for small-scale, uncomplicated indoor environments. Line collection involves setting known control points and the lines connecting these points, with data collectors traversing these lines. The collectors' location is determined through PDR and control points. Although this method is more efficient than point collection, the precision of control points significantly impacts the accuracy of data collection, making the selection of control points crucial. However, not all environments are conductive for establishing control points, and the number of control points often increases with the collection area, similar to point collection, limiting its applicability to compact indoor environments.

Crowdsourcing does not depend on control points and manual calibration, making it suitable for large areas. However, its accuracy is lower than that of point and line collection. Currently, numerous studies have been conducted on constructing magnetic field maps through crowdsourcing. For instance, Luo processed

crowdsourced data by clustering magnetic field trajectories using geomagnetic signal observation models (Luo et al., 2017). Chen constructed magnetic field maps by merging multi-user paths and using the Dynamic Time Warping (DTW) for location correction (Chen et al., 2020). Nonetheless, crowdsourcing requires substantial user data for clustering and stitching, and it is primarily applicable to public areas. In specialized domains, the limited data due to low foot traffic may not satisfy the requirements for crowdsourcing.

SLAM leverages the similarity of magnetic field to construct loop constraints, facilitating globally consistent trajectory estimation. This approach does not require pre-planning or the measurement of numerous control points, thus reducing the demand for coordinate measurement. Currently, SLAM-based magnetic field map generation methods primarily include graph optimization and particle filtering. Gao proposed a magnetic field map generation method based on graph optimization, where the front end detects loop closures using magnetic field observations, and the back end solves the pose graph optimization problem, refining the trajectory for global consistency(Gao and Harle, 2017). Osman(Osman et al., 2022), Gao(Gao and Harle, 2018), and Kok(Kok and Solin, 2018) proposed particle filter-based magnetic field map generation methods that utilizes the similarity of magnetic field features for loop closure detection, integrating magnetic field loop closures and linear constraints into the filtering process to adjust particle weights. To enhance particle filter performance, some studies employ backtracking algorithms to improve filtering efficiency by combining map information to eliminate ineffective particles and retain effective particles for increased precision. Cock use PDR and building floor plans as prior information(De Cock et al., 2021). When particles enter dead-ends, they are considered invalid and replaced with valid particles to recalculate and generate trajectories. Zhang imposes constraints on the historical positions and feasible regions of particles and applies backtracking to newly generated particles, ensuring their validity(Zhang et al., 2023). The aforementioned backtracking schemes rely on the assistance of building maps. However, building maps are often not readily accessible.

3. System Overview

The generation of a magnetic field map involves acquiring the distribution of environmental magnetic field within indoor areas, necessitating the establishment of a correspondence between magnetic field strength and location. Given that environmental characteristics remain consistent at the same location, sensor-extracted environmental features can identify previously visited locations, where successful identification is termed a successful loop closure. Loop constraints can thus be employed to mitigate error drift. Evidently, during the generation of magnetic field map, magnetic field strength serves as readily available environmental characteristics without the need for additional attributes. Consequently, the core idea of this study is to utilize a particle filter framework, employing pedestrian walking trajectories as prior information and magnetic field fingerprint features for loop detection as observations, which aims to suppress position drift, facilitating trajectory convergence. Ultimately, particle backtracking is applied to eliminate ineffective particles, resulting in a trajectory with improved convergence.

The system algorithm framework for the proposed magnetic field map generation method is depicted in Figure 1. The system comprises three primary modules: the Particle Filtering module, the Position and Attitude Estimation module, and the Map Gridding module. The Particle Filtering module is primarily responsible for estimating pedestrian positions. Pedestrian position estimation can be represented by a set of particles derived from Bayesian posterior probabilities, which adjust the overall estimation as observational data, specifically loop closure detection in this paper. The process of position estimation based on particle filtering involves: Firstly, initializing the grid and particles, then predicting the pedestrian's motion state using a motion model, and progressively expanding the grid map based on this prediction. Maintaining state prediction and grid map expansion until observations are received. Upon detecting a loop closure, particle weights are updated, and when the number of loop closure particles is sufficient, particle backtracking and trajectory reconstruction are performed. Subsequently, particle resampling occurs when particle depletion conditions are met. Finally, the map is updated, with particles updating based on observational data and recording each feature in the map.

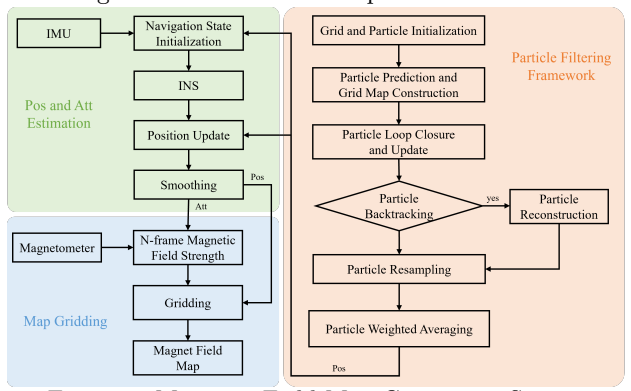


Figure 1. Magnetic Field Map Generation System Framework

The Particle Filtering module provides position correction information for the Position and Attitude Estimation module. Due to the low precision of MEMS-IMUs built in smartphones, the accuracy of inertial navigation states is low. Position correction yields relatively reliable position and attitude information. After obtaining the smartphone's attitude, the magnetic field strength can be transformed to the navigation frame (n-frame), and associated with the smartphone's position, establishing the correspondence between magnetic field and location. Ultimately, the area covered by the position is gridded, resulting in a magnetic field grid map.

4. Magnetic Field Grid Map Generation Based on Particle Filtering

In this section, we primarily introduce the algorithmic components of grid map generation based on particle filtering. The main components include particle prediction and grid map construction, particle loop closure and updating, particle backtracking and trajectory reconstruction, and particle resampling for how particle filtering is employed for pedestrian position estimation.

Additionally, trajectory alignment and grid magnetic field map generation are discussed concerning how the pedestrian positions estimated by particle filtering are used to generate a magnetic field grid map.

4.1 Particle Prediction and Particle Grid Map Construction

The position estimation of pedestrians can be represented by a set of Bayesian posterior probability particles, whose weights are adjusted with the update of observations, thereby refining the overall estimation. Similar to the Kalman filter, the particle filter also comprises prediction and observation phases. During the particle prediction phase, the pedestrian's motion model is employed to forecast the trajectory of the particles, generating a predicted state for each particle, which can be written as

$$p\left(\boldsymbol{x}_{t}|\boldsymbol{x}_{t-1},\ \boldsymbol{u}_{t}\right),\tag{1}$$

where \boldsymbol{x}_t and \boldsymbol{x}_{t-1} represent the pedestrian's position at the t-th epoch and the (t-1)th epoch, respectively; \boldsymbol{u}_t denotes the control variable. In this paper, the forward relative displacement and heading increment of the pedestrian, as provide by PDR, are utilized to predict the pedestrian's position, which can be expressed as

$$\begin{cases}
\mathbf{x}_{k} = \begin{bmatrix} \mathbf{r}_{k-1} + \Delta \mathbf{r}_{k} + \varepsilon_{k}^{r} \\ \Delta \psi_{k} \odot \psi_{k-1} \odot \exp_{\psi} \left(\varepsilon_{k}^{\psi} \right) \end{bmatrix} \\
\begin{bmatrix} \varepsilon_{k}^{r} \\ \varepsilon_{k}^{\psi} \end{bmatrix} \sim \mathbf{N} \left(0, \sigma^{2} \right)
\end{cases} (2)$$

where Δr_k denotes the increment in relative displacement; $Delta\psi_k$ is the heading increment; ε_k^r and ε_k^{ψ} represent Gaussian perturbations with a mean of zero added to each particle. During prediction, the particles exhibit a divergent state.

As pedestrians move in indoor environments, the magnetic field strength within each grid is recorded as they traverse, gradually filling the grid map as their trajectory extends. Due to the inherent inaccuracies in the heading determined by PDR, this paper utilizes the horizontal and vertical components as feature quantities, instead of the triaxial magnetic field strength. The horizontal and vertical components can be calculated as

$$\begin{cases}
\mathbf{M}^{b} = \begin{bmatrix} m_{x} & m_{y} & m_{z} \end{bmatrix}, & \mathbf{M} = \begin{bmatrix} m_{h} & m_{v} \end{bmatrix} \\
\|m\| = \sqrt{m_{x}^{2} + m_{y}^{2} + m_{z}^{2}} \\
m_{v} = -\sin\theta \cdot m_{x} + \sin\phi\cos\theta m_{y} + \cos\phi\cos\theta m_{z} \\
m_{h} = \sqrt{\|m\| - m_{v}^{2}}
\end{cases} (3)$$

where M^b represents the triaxial raw observations from the magnetometer; m_h and m_v denote the horizontal and vertical components of the magnetic field, respectively; $\|m\|$ is the magnitude of the magnetic field; The pitch angle θ and roll angle ϕ can be derived from accelerometer levelling. Meanwhile, due to the introduction of random perturbations to each particle, the trajectory of each particle and the magnetic field map are distinct. When a particle's trajectory extends beyond the $N \times N$ grid-covered region, it is necessary to appropriately expand the grid.

4.2 Particle Loop Closure and Updating

Given that the accumulation of errors in PDR, we employ path looping to construct observational conditions to minimize errors without additional devices. Consequently, the data collectors are required to walk along a fixed trajectory multiple times to create loop conditions. Theoretically, as long as the number of particles is sufficiently large, at least one particle will return to its original position, ensuring the occurrence of particle looping.

To further ensure the reliability and accuracy of loop detection, several criterial must be established. The procedure involves checking whether the grid currently accessed by the particle has been visited previously, with an interval time greater than a certain threshold. Subsequently, a similarity comparison of the magnetic field sequences is performed. This involves comparing the sequence stored at the t-th epoch to the (t-m)-th epoch with that at the k-th epoch to the (k-m)-th epoch, using Pearson correlation coefficient and Euclidean distance as metrics, which can be written as

$$\begin{cases}
\mathbf{R}_{xy} = \frac{\sum_{i=1}^{m} \left(\mathbf{X}_{i} - \bar{\mathbf{X}}\right) \left(\mathbf{Y}_{i} - \bar{\mathbf{Y}}\right)}{\sqrt{\sum_{i=1}^{m} \left(\mathbf{X}_{i} - \bar{\mathbf{X}}\right)^{2}} \sqrt{\sum_{i=1}^{m} \left(\mathbf{Y}_{i} - \bar{\mathbf{Y}}\right)^{2}}} \\
Dis = \sum_{i=1}^{m} \left(\mathbf{X}_{i} - \mathbf{Y}_{i}\right)^{2}
\end{cases} (4)$$

where \mathbf{R}_{xy} and Dis represent Pearson's coefficient and Euclidean distance, respectively. X and Y denote the two sequences to be compared; X_i is the *i*-th value in the sequence X. A higher R_{xy} signifies greater sequence correlation, while a smaller Dis indicates higher correlation. m denotes the length of the magnetic field sequence, which is typically set to approximately 10-20, corresponding to a length of approximately 10 m, due to the low-frequency nature of the magnetic field. If the similarity conditions for the magnetic field sequences are met, the grid is determined to be a revisited grid. When N_{thes} out N of consecutive grids are identified as revisited grids, a loop is successfully detected. Figure 2 illustrates the process of particle revisits. Different colors represent the walking paths of pedestrians indicated by various particles, with the red path indicating a particle revisit.

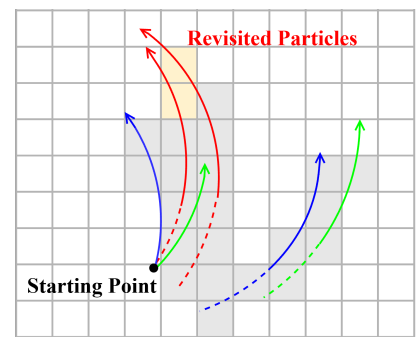


Figure 2. the Process of Particle Revisits

Upon the successful loop detection, it is necessary to update the weight of the particle, which can be expressed

$$w_t^i = w_{t-1}^i \frac{N_c}{N_p} \exp\left(RMSE\left(V_c\right)\right), \ N_c \ge N_{thes} \quad (5)$$

where w_t^i and w_{t-1}^i are the weights of particle at the t-th

epoch and the (t-1)-th epoch, respectively; N_p and N_c represent the number of grid windows considered for revisits and the number of grids satisfying the revisit condition, respectively; V_c denotes the set of similarity values for all grids meeting the revisit condition; $RMSE\left(\cdot\right)$ is the root mean square error (RMSE) of the set. Additionally, the weight must be normalized, and upon completion of normalized, a weighted average of the particles is performed to output the estimated value for the current epoch.

4.3 Particle Backtracking and Trajectory Reconstruction

In indoor environments, pedestrian trajectories are frequently restricted by various factors, primarily due to impassable paths formed by the arrangement of indoor furniture and walls. Consequently, when employing particle filtering for pedestrian position estimation, it is possible to filter and exclude particles based on actual conditions to enhance computational precision. For instance, if a particle is detected to cross furniture or walls, which is inconsistent with logical scenarios, it should be considered invalid and removed. The pedestrian trajectory estimation is then recalculated based on the remaining valid particles.

The data collection scheme in this paper necessitates that collectors walk along a prescribed route multiple times to meet loop construction conditions. Hence, particles that do not form loops should be deemed invalid and excluded. When loop closure is successfully identified, particles can be corrected. However, there are periods lacking observational information in practical scenarios, such as walking in previously unexplored areas. During these times, particles may diverge, and even when observational information becomes available again, only the current particles can be corrected, while historical particles remain fixed, deteriorating the global consistency of the trajectory. As shown in Figure 3, when walking along the path 1-2-3-4-1-2-3-4-5-6-7-8, there are shared edges in the small loop regions that satisfy the objective loop conditions. Ideally, as shown in subfigure (a), small loops in local regions should maintain consistency. However, due to the lack of observational information while walking along 5-6-7-8_1, the particle trajectory estimates diverge. Although loop observational information corrects the current particles upon reaching path 8, the historical particles remain fixed and cannot be adjusted.

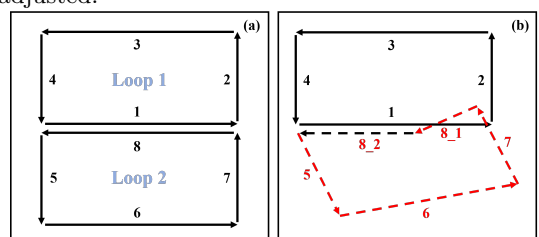


Figure 3. Schematic of Particle Loop Closure

Therefore, it is essential to regenerate trajectories by discarding invalid particles and retaining valid ones, a process known as particle backtracking. The specific procedure is as follows: First, upon updating all particles at a given epoch, the system quantifies the number of particles that have generated loop observations and records the temporal information. When the pro-

"Mobile Mapping for Autonomous Systems and Spatial Intelligence", 20-22 June 2025, Xiamen, China

portion of observed particles reaches N% of the total particle population, the temporal verification phase is initiated. The current timestamp is evaluated against the previous backtracking time. if the differential exceeds a predetermined threshold, the backtracking process commences. Particle weights are arranged in descending order, with the upper m% preserved and the lower m% eliminated. The correlation between m and N is m = 2N. This approach ensures the retention of particles generating loop observations while maintaining a subset of non-generating particles, thereby minimizing trajectory discontinuities and preserving continuity. Subsequently, new trajectories are reconstructed from the retained particles, replacing the original paths from the current timestamp to the previous backtracking point. In this paper, m is configured at 30 and n at 15. After backtracking, Gaussian perturbations are applied to the remaining particles to maintain population diversity before proceeding to the subsequent epoch's particle prediction and update phase. Figure 4 demonstrates the trajectory comparison before and after backtracking implementation. It can be observed that after backtracking, the red dashed line regenerates the path segment 5-6-7, maintaining overall consistency compared to the blue path.

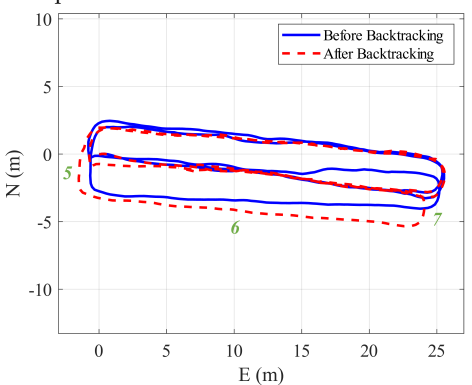


Figure 4. Comparison of Trajectories before and after backtracking

4.4 Particle Resampling

After several iterations of loop observations, a small number of particles typically acquire larger weights, while the majority are assigned smaller weights, leading to the particle impoverishment. Particles with smaller weights contribute minimally to the system's estimation. To address this problem, it is necessary to increase the number of particles with larger weights and decrease those with smaller weights, which requires resampling the particles. The number of samples for each particle is determined by its corresponding weight, meaning particles with larger weights are sampled more frequently, while those with smaller weights are sampled less. Additionally, it is essential to assess the deviation of particle weights to determine whether resampling is required, and the criterion for this assessment can be expressed as

$$N_{eff} = \frac{1}{\sum_{i=1}^{N} (w^i)^2} \tag{6}$$

where N_{eff} is the threshold for resampling, and a smaller N_{eff} indicates more severe degradation. Subsequently, the cumulative probability C_i is calculated to transform the originally weighted samples $\left\{\boldsymbol{x}_t^i, w_t^i\right\}_{i=1}^N$ into equally

weighted samples $\left\{\tilde{\boldsymbol{x}}_t^i, 1/N\right\}_{i=1}^n$.

4.5 Trajectory Alignment

The loop trajectory obtained after particle back-tracking is relatively consistent in shape with the true trajectory, exhibiting translation, rotation, and scale as the three error components. To correct this, four known position coordinates need to be marked on the map. As illustrated in Figure 5, the black line represents the true trajectory, while the grey line depicts the loop closure trajectory. The loop trajectory is aligned with the true trajectory by four known points.

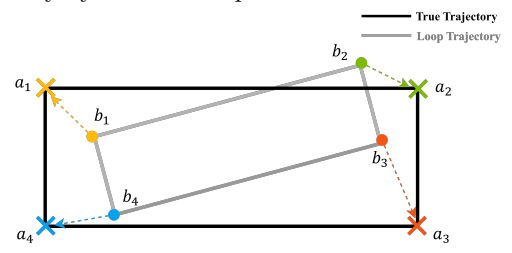


Figure 5. Loop Closure Trajectory Alignment to True Trajectory

Given a set of coordinates $\mathbf{A} = \begin{bmatrix} a_1 & a_2 & a_3 & a_4 \end{bmatrix}$ from the true trajectory that are not collinear and are widely dispersed, and a corresponding set of coordinates $\mathbf{B} = \begin{bmatrix} b_1 & b_2 & b_3 & b_4 \end{bmatrix}$ from the loop closure trajectory, the requirement is that $\mathbf{A} = \mathbf{R}\mathbf{B} + \mathbf{t}$, where \mathbf{R} encompasses the rotation and scale factors, and \mathbf{t} is the translation vector. Therefore, the trajectory alignment can be transformed into solving for \mathbf{R} and \mathbf{t} .

First, calculate the centroid coordinates of A and B, denoted as C_A and C_B , respectively. Subtract each centroid from all points in A and B to eliminate the effect of translation, which can be written as

$$\begin{cases}
A' = A - C_A \\
B' = B - C_B
\end{cases}$$
(7)

where A' and B' only maintain the relationship A' = RB' after removing the translation effect. Since the points in B are not collinear, the least squares method can be used to determine R, which can be written as

$$\boldsymbol{R} = \boldsymbol{A'}\boldsymbol{B'}^T \left(\boldsymbol{B'}\boldsymbol{B'}^T\right)^{-1} \tag{8}$$

Meanwhile, since A = RB + t also holds for the centroid coordinates C_A and C_B , the calculation of the translation vector t can be expressed as

$$t = C_A - RC_B \tag{9}$$

4.6 Grid Magnetic Field Map Generation

Given that the inability of surveyors to ensure uniformly high-density magnetic field feature collection, it is necessary to encrypt the magnetic field feature to generate a uniformly distributed magnetic field map. Since the distribution of the environmental magnetic field is relatively smooth, it can be assumed that the intensity changes linearly with distance, and interference from ferromagnetic materials on the environmental magnetic field is confined to small areas. Therefore, a uniform magnetic field grid map can be generated through gridding and linear interpolation (Kuang et al., 2021).

5. Experiments and Results

5.1 Experimental Setting

To validate the accuracy of map generation of the proposed particle filtering-based magnetic field map generation method, two tests were conducted in Xinghu Building at Wuhan University. The test areas are the 17th floor public area and the underground parking lot (B1) of the building, representing typical indoor pedestrian positioning scenarios. The experimental areas are indicated by the red diagonal lines shown in Figure 6. Due to the small size of the public area on the 17th floor of the Xinghu Building, loops are easily formed, and data collection was conducted by walking directly along the outer perimeter. The underground parking area is larger. Thus, during data collection, the area was first divided into several smaller sub-regions with shared common edges. Multiple laps were walked along the outer perimeter of the entire area to ensure sufficient loop closure of the trajectory, and then data for each sub-region were collected. The magnetic field map of the entire area was constructed using the common edges and the backtracking algorithm.

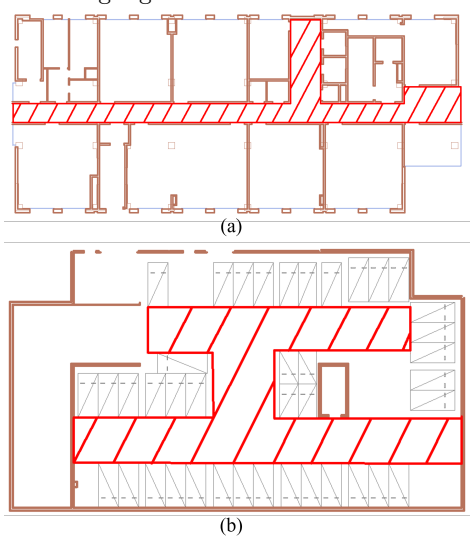


Figure 6. CAD Drawing of the Test Area. (a) 17th Floor of the Xinghu Building (b) Underground Parking Lot of the Xinghu Building

The accuracy of the magnetic field generation is evaluated in two aspects: first, by assessing the accuracy of the trajectories used to generate the map, and second, by comparing the generated magnetic field map with the one constructed by Foot-INS.

5.2 Loop Closure Trajectory Comparison

Figure 7 illustrates the PDR trajectories, the trajectories incorporating loop closure constraints, and the trajectories resulting from the integration of loop closure constraints with historical state backtracking within the test areas. It can be observed that the PDR trajectories (depicted as black paths in the figure) exhibit a growing positional error as the walking distance increases, attributable to continuous heading divergence. The loop closure constraints effectively suppress the positional error caused by heading divergence to some extent. On this basis, the historical state backtracking method leverages the advantages of data post-processing to further improve the precision of trajectory estimation.

Figure 8 presents the trajectories before and after alignment using four control points, in addition to the depiction of the control points themselves. The selected control points are relatively dispersed and noncolinear. It is evident that the aligned trajectories closely match the reference trajectories. Additionally, the error between the aligned and reference trajectories was calculated for both scenarios, with the RMS positional errors being 1.13 m and 1.21 m for the 17th floor and B1 floor, respectively. The errors corresponding to the 68% are 0.99 m and 1.32 m, while the errors corresponding to the 95% are 2.10 m and 2.20 m. The magnetic field maps derived from these trajectories meet the requirements for meter-level magnetic field matching positioning.

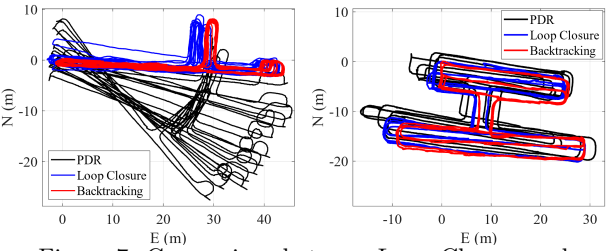


Figure 7. Comparison between Loop Closure and Backtracking. (a) 17th Floor of the Xinghu Building (b) Underground Parking Lot

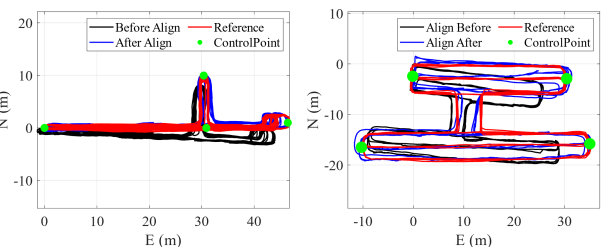


Figure 8. Comparison of Trajectory Alignment Before and After. (a) 17th Floor of the Xinghu Building (b) Underground Parking Lot of the Xinghu Building

5.3 Magnetic Field Map Results

This study employs pedestrian location and attitude estimation using PDR, constrained by loop closure and historical state backtracking methods, to correlate with magnetic field strength for generating a magnetic field map as the evaluation sample. The reference map is generated by associating pedestrian location and attitude estimated by P-POS with magnetic field strength. Figure 9 and 10 display the comparative results for three directional components of the magnetic field maps in two test areas. The figures demonstrate that the proposed method closely aligns with the P-Pos generated magnetic field maps in the north, east, and vertical components of the magnetic field.

	17th Floor (mGauss)			Parking Lot (mGauss)		
	RMS	68%	95%	RMS	68%	95%
North	33.2	19.9	75.2	31.2	22.0	63.7
East	28.4	21.4	53.1	33.9	33.1	59.8
Vertical	22.8	19.0	48.1	45.3	44.8	79.9

Table 1. Error Statistics of the Magnetic Field Map.

A quantitative analysis was performed by subtracting the reference values from the maps generated by the proposed method. The results, as illustrated in Figure 11 and 12, reveal that in most areas, the magnetic field differences are within 50 mGauss, with some re-

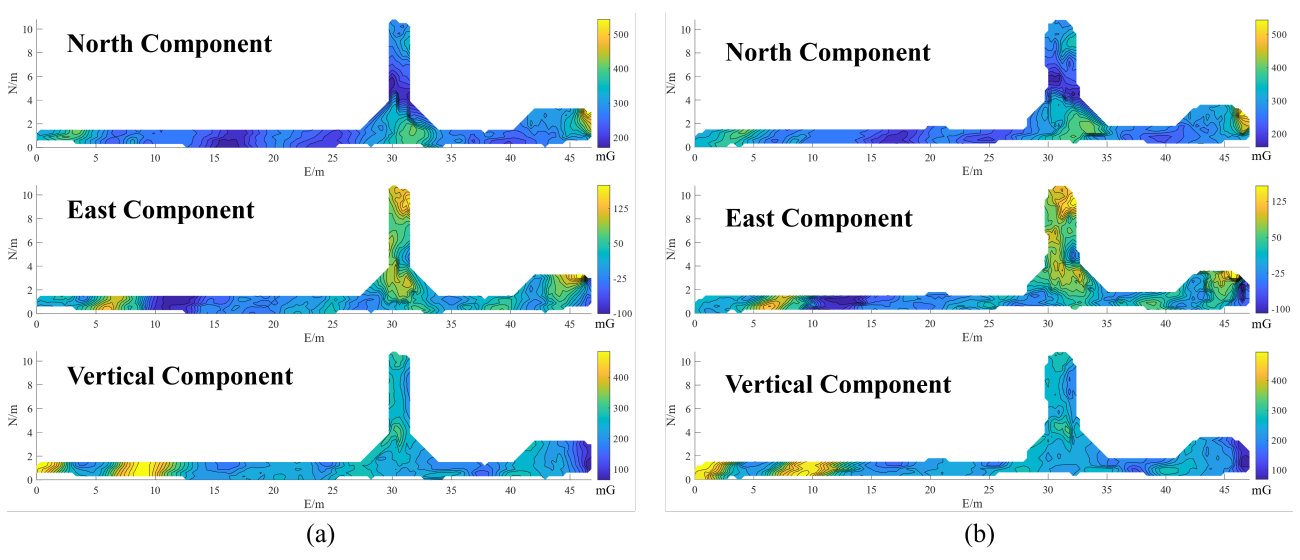


Figure 9. Magnetic Field Map of the 17th of Xinghu Building (North, East, and Vertical Components, mGauss). (a)
Reference, (b) Generated by the Proposed Method in this Paper

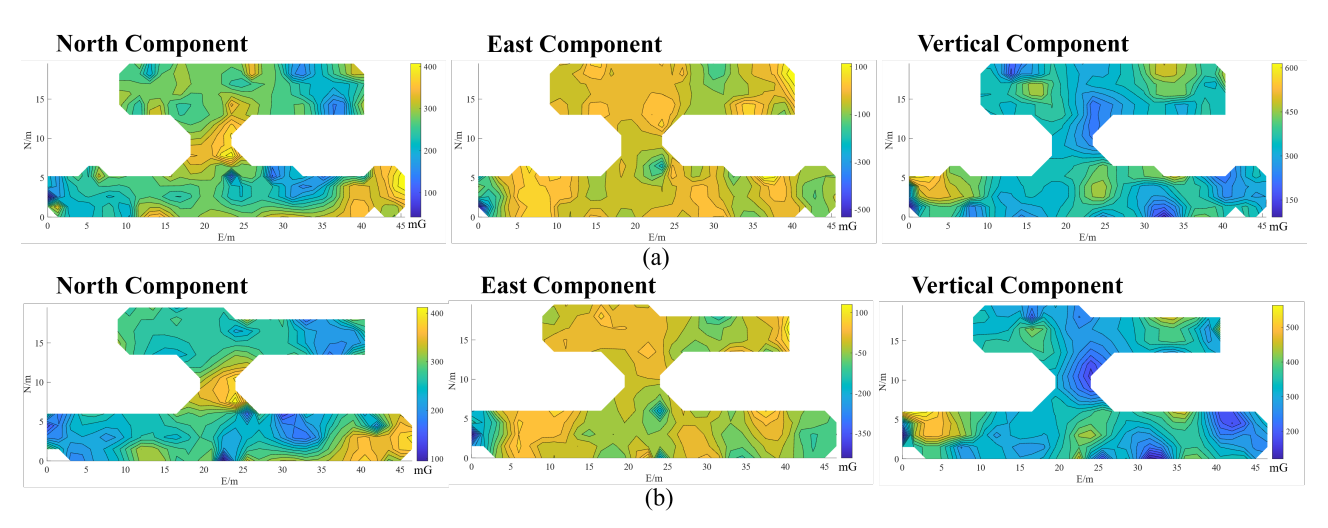


Figure 10. Magnetic Filed Map of the Underground Parking Lot (North, East, and Vertical Components, mGauss). (a)
Reference, (b) Generated by the Proposed Method in this Paper

gions near the map edges reaching 200 mGauss. These areas are walls and columns, containing ferromagnetic materials like rebar, acting as sources of magnetic interference where the magnetic field decays rapidly, necessitating high positional accuracy. Since these areas are relatively small and not typical pedestrian pathways (pedestrians generally avoid walking close to walls and columns), the impact on pedestrian positioning is minimal. Table 1 summarizes the errors in the magnetic field maps generated by the proposed method. The statistical results indicate that the magnetic filed map errors for the two test areas range between 30 and 40 mGauss (RMS), approximately one-tenth of the indoor magnetic field fluctuations, suggesting that from a signal-to-noise ratio perspective, there will not be a significant decline in positioning performance due to magnetic field feature matching.

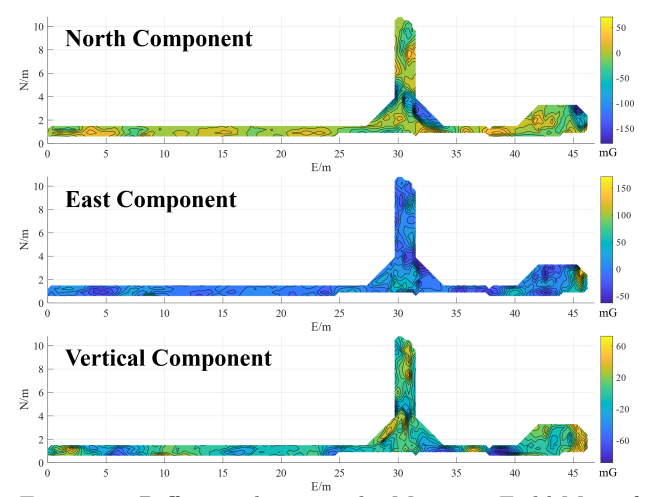


Figure 11. Difference between the Magnetic Field Map of the 17th Floor of Xinghu Building and Reference (North, East, and Vertical Components, mGauss)

"Mobile Mapping for Autonomous Systems and Spatial Intelligence", 20-22 June 2025, Xiamen, China

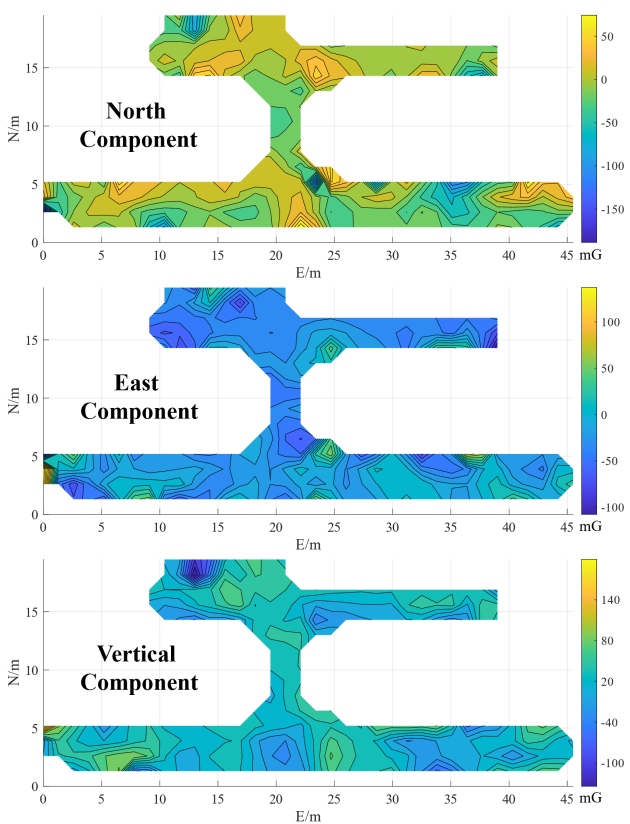


Figure 12. Difference between the Magnetic Field Map of the Underground Parking Lot and Reference (North, East, and Vertical Components, mGauss)

6. Conclusion and Future Work

This paper proposed a particle filtering-based magnetic field map generation method, addressing the complexity and cost limitations of existing techniques. By necessitating repeated traversals of collection routes, the method leverages PDR for initial trajectory estimation and employs the horizontal and vertical components of the magnetic field to automatically identify revisits to previously traversed paths, thereby mitigating positional error accumulation. A notable contribution is the backtracking of historical particle states during postprocessing, improving trajectory heading convergence and estimation precision. The relative trajectory is calibrated utilizing non-collinear control points and bilinear interpolation to generate a gridded magnetic field map. Experiments demonstrate the proposed method's capability to estimate trajectories with RMS errors below 1.3 m, fulfilling the requirements for meter-level magnetic field matching. The generated magnetic field map exhibits errors within the 30-40 mGauss in the north, east, and vertical directions.

The method's effectiveness and cost-effectiveness enable widespread applications, particularly for indoor smartphone navigation in GNSS-denied environments like shopping malls and underground facilities. Nevertheless, several limitations warrant further investigation. Firstly, to accommodate various pedestrian smartphoneholding modes, future work will encompass data collection across various modes, including swinging and calling, extending beyond the current flat smartphoneholding mode. Additionally, the particle filtering al-

gorithm requires enhancement; integrating structural information, such as architectural floor plans or designated non-traversable regions, could facilitate intelligent pruning or elimination of invalid particles, thereby augmenting the precision and reliability of trajectory generation.

References

Ashraf, I., Zikria, Y. B., Hur, S., Park, Y., 2020. A Comprehensive Analysis of Magnetic Field Based Indoor Positioning With Smartphones: Opportunities, Challenges and Practical Limitations. IEEE Access, 8, 228548–228571. Conference Name: IEEE Access.

Campos, C., Elvira, R., Rodríguez, J. J. G., M. Montiel, J. M., D. Tardós, J., 2021. ORB-SLAM3: An Accurate Open-Source Library for Visual, Visual–Inertial, and Multimap SLAM. IEEE Transactions on Robotics, 37(6), 1874–1890. Conference Name: IEEE Transactions on Robotics.

Chen, L., Wu, J., Yang, C., 2020. MeshMap: A Magnetic Field-Based Indoor Navigation System With Crowdsourcing Support. IEEE Access, 8, 39959–39970. Conference Name: IEEE Access.

De Cock, C., Joseph, W., Martens, L., Trogh, J., Plets, D., 2021. Multi-Floor Indoor Pedestrian Dead Reckoning with a Backtracking Particle Filter and Viterbi-Based Floor Number Detection. Sensors, 21(13), 4565. Number: 13 Publisher: Multidisciplinary Digital Publishing Institute.

Galván-Tejada, C. E., García-Vázquez, J. P., Brena, R. F., 2014. Magnetic Field Feature Extraction and Selection for Indoor Location Estimation. Sensors, 14(6), 11001–11015. Number: 6 Publisher: Multidisciplinary Digital Publishing Institute.

Gao, C., Harle, R., 2017. MSGD: Scalable back-end for indoor magnetic field-based GraphSLAM. 2017 IEEE International Conference on Robotics and Automation (ICRA), 3855–3862.

Gao, C., Harle, R., 2018. Semi-Automated Signal Surveying Using Smartphones and Floorplans. IEEE Transactions on Mobile Computing, 17(8), 1952–1965. Conference Name: IEEE Transactions on Mobile Computing.

Guo, X., Ansari, N., Hu, F., Shao, Y., Elikplim, N. R., Li, L., 2020. A Survey on Fusion-Based Indoor Positioning. IEEE Communications Surveys & Tutorials, 22(1), 566–594. Conference Name: IEEE Communications Surveys & Tutorials.

Huang, L., 2021. Review on LiDAR-based SLAM Techniques. 2021 International Conference on Signal Processing and Machine Learning (CONF-SPML), 163–168.

Jianyong, Z., Haiyong, L., Zili, C., Zhaohui, L., 2014. RSSI based Bluetooth low energy indoor positioning. 2014 International Conference on Indoor Positioning and Indoor Navigation (IPIN), 526–533.

Kok, M., Solin, A., 2018. Scalable Magnetic Field SLAM in 3D Using Gaussian Process Maps. 2018 21st International Conference on Information Fusion (FUSION), 1353–1360.

- Kuang, J., Li, T., Chen, Q., Zhou, B., Niu, X., 2023. Consumer-Grade Inertial Measurement Units Enhanced Indoor Magnetic Field Matching Positioning Scheme. IEEE Transactions on Instrumentation and Measurement, 72, 1–14. Conference Name: IEEE Transactions on Instrumentation and Measurement.
- Kuang, J., Li, T., Niu, X., 2021. An Efficient and Robust Indoor Magnetic Field Matching Positioning Solution Based on Consumer-Grade IMUs for Smartphones. C. Yang, J. Xie (eds), China Satellite Navigation Conference (CSNC 2021) Proceedings, Springer, Singapore, 535–545.
- Kuang, J., Niu, X., Zhang, P., Chen, X., 2018. Indoor Positioning Based on Pedestrian Dead Reckoning and Magnetic Field Matching for Smartphones. Sensors, 18(12), 4142. Number: 12 Publisher: Multidisciplinary Digital Publishing Institute.
- Liu, G., Yu, B., Huang, L., Shi, L., Gao, X., He, L., 2021. Human-Interactive Mapping Method for Indoor Magnetic Based on Low-Cost MARG Sensors. IEEE Transactions on Instrumentation and Measurement, 70, 1–10. Conference Name: IEEE Transactions on Instrumentation and Measurement.
- Luo, H., Zhao, F., Jiang, M., Ma, H., Zhang, Y., 2017. Constructing an Indoor Floor Plan Using Crowdsourcing Based on Magnetic Fingerprinting. Sensors, 17(11), 2678. Number: 11 Publisher: Multidisciplinary Digital Publishing Institute.
- Osman, M., Viset, F., Kok, M., 2022. Indoor SLAM using a foot-mounted IMU and the local magnetic field. 2022 25th International Conference on Information Fusion (FUSION), 1–7.
- Ouyang, G., Abed-Meraim, K., 2022. A Survey of Magnetic-Field-Based Indoor Localization. Electronics, 11(6), 864. Number: 6 Publisher: Multidisciplinary Digital Publishing Institute.
- Tinh, P. D., Hoang, B. H., 2022. Wifi Indoor Positioning with Genetic and Machine Learning Autonomous War-Driving Scheme. IJACSA, 13(2).
- Zhang, X., Zhou, T., Wang, J., Wang, T., Zhao, H., 2023. An Improved Particle Filter Map Matching Algorithm for Personal Inertial Positioning. Journal of Computer and Communications, 11(6), 103–112. Number: 6 Publisher: Scientific Research Publishing.